Supplementary Material for:

Streams, cascades, and pools: Various water cluster motifs in structurally similar Ni(II) complexes

Nina Saraei,[1] Oleksandr Hietsoi,[1] Christopher S. Mullins,[1] Alexander J. Gupta,[2] Brian C. Frye,[1] Mark S. Mashuta,[1] Robert M. Buchanan,[1]* Craig A. Grapperhaus[1]*

[1]Department of Chemistry, University of Louisville, Louisville, 40292, USA
[2]Department of Chemical Engineering, University of Louisville, Louisville, 40292, USA

Table of Contents

Figure S1. ^{1}H NMR of HL^1: (DMSO - D_6), 400 MHz) δ 2.05 (br, 2H), 2.63 (t, 2H), 3.28 (t, 2H), 3.98 (s, 3H), 6.82 (d, 1H), 6.88 (d, 1H), 8.14 (s, 1H). The small peak labeled x results from tautomerization of the amido proton (d). Addition of D_2O results in the loss of this peak. S3

Figure S2. ^{1}H NMR of H_2L^3: S3

Figure S3. ^{1}H NMR of NiL^3 (**2**): (CD_3OD, 400 MHz) δ 1.18 (s, 1H), 2.16-3.45 (m, 8H), 3.78 (s, 3H), 6.29 (d, 1H), 6.92 (d, 1H). S4

Figure S4. ^{1}H NMR of NiL^4 (**4**): (C_3D_6O, 400 MHz) δ 1.77 (s, 3H), 1.90 (s, 3H), 2.84 (t, 2H), 3.41 (t, 2H), 3.92 (s, 3H), 4.98 (s, 1H), 6.61 (d, 1H), 7.05 (d, 1H). S4

Figure S5. ^{1}H NMR of NiL^5 (**5**): ($CDCl_3$, 400 MHz) δ 1.78 (s, 3H), 1.82 (s, 3H), 2.92 (t, 2H), 3.45 (t, 3H), 3.88 (s, 3H), 4.86 (s, 1H), 6.62 (d, 1H), 6.64 (d, 1H). S5

Figure S6. UV-Vis spectrum of NiL^3 (**2**) in CH_3CN. S5

Figure S7. UV-Vis spectrum of Ni(L^1)$_2$ (**3**) in CH_2Cl_2. ....S6

Figure S8. UV-Vis spectrum of NiL^4 (**4**) in CH_3CN. S6

Figure S9. UV-Vis spectrum of NiL^5 (**5**) in CH_3CN. S7

Table S1. Selected stretches (cm^{-1}) in FT-IR spectra of HL^1 and **1-5**. S7

Figure S10. FT-IR spectrum of HL^1. ....S8

Figure S11. FT-IR spectrum of NiL^2 (**1**). S8

Figure S12. FT-IR spectrum of NiL^3 (**2**). S9

Figure S13. FT-IR spectrum of Ni(L^1)$_2$ (**3**). S9

Figure S14. FT-IR spectrum of NiL^4 (**4**). S10

Figure S15. FT-IR spectrum of NiL^5 (**5**). S10

Figure S16. MALDI of NiL^3 (**2**). S11

Figure S17. MALDI of Ni(L^1)$_2$ (**3**). S11

Figure S18. MALDI of NiL^4 (**4**). S12

Figure S19. MALDI of NiL^5 (**5**). S12

Figure S20. Unit cell diagram of NiL^3 (**2**). S13

Figure S21. Unit cell diagram of Ni(L^1)$_2$ (**3**). S13

Figure S22. Unit cell diagram of NiL^4 (**4**). S14
Figure S23. Unit cell diagram of NiL^5 (**5**). S14
Figure S24. TGA of NiL^2 (**1**). S15
Figure S25. DSC of NiL^2 (**1**). S15
Figure S26. TGA of NiL^3 (**2**). S16
Figure S27. DSC of NiL^3 (**2**). S16
Figure S28. TGA of NiL^4 (**4**). S17
Figure S29. DSC of NiL^4 (**4**). S17
Figure S30. TGA of NiL^5 (**5**). S18
Figure S31. DSC of NiL^5 (**5**). S18
Figure S32. $C^2_2(12)$ HB motif in $Ni(L^1)_2$ (**3**). S19
Figure S33. Bode representations of EIS data for 22 μF capacitor control (A), complexes 1 (B), 4 (C), and 5 (D). Shows the phase angle and impedance behavior as a function of frequency. The inverse relation between Z and frequency and constant ~90 ° phase angles in all four plots are characteristics of capacitors. S19
Table S2. Capacitances (with associated chi-squared values) and Z' at 100 kHz (indicative of equivalent series resistance) for the capacitor control and complexes **1**, **4**, and **5** at various applied DC biases. Also depicted is the equivalent circuit model used to fit EIS data and determine capacitance. S20
Figure S34. Nyquist representations of EIS data for 22 μF capacitor control (A), complexes 1 (B), 4 (C), and 5 (D). Data in B, C, and D were truncated at -Z'' = 80,000 Ω to illustrate similarities with (A) and omit the diffusion-related noise observed at low frequencies. S21

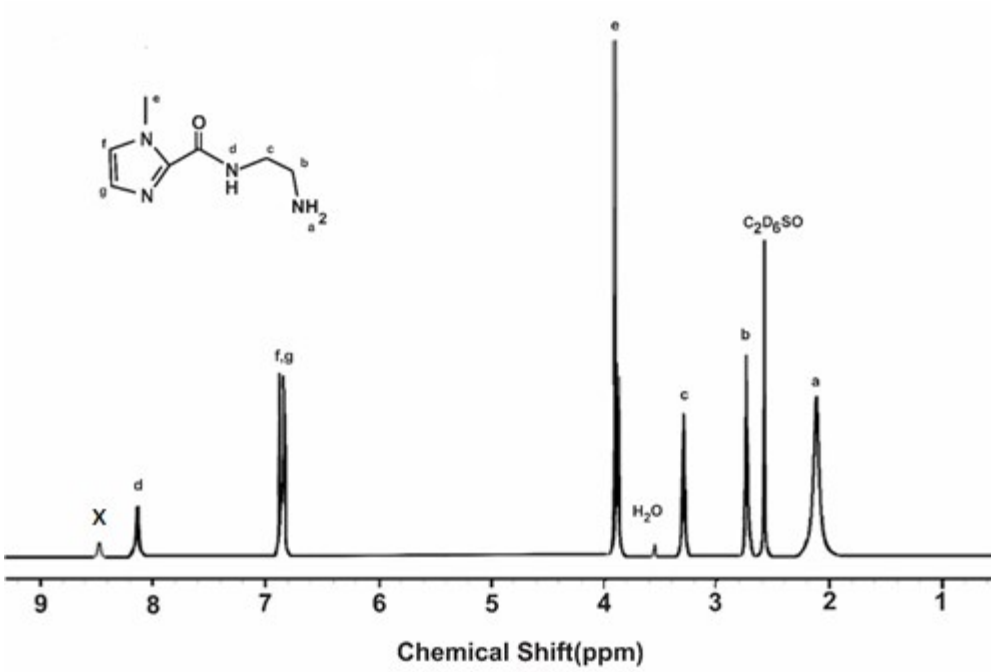

Figure S1. ^{1}H NMR of HL[1]: (DMSO - D_6), 400 MHz) δ 2.05 (br, 2H), 2.63 (t, 2H), 3.28 (t, 2H), 3.98 (s, 3H), 6.82 (d, 1H), 6.88 (d, 1H), 8.14 (s, 1H). The small peak labeled x results from tautomerization of the amido proton (d). Addition of D_2O results in the loss of this peak.

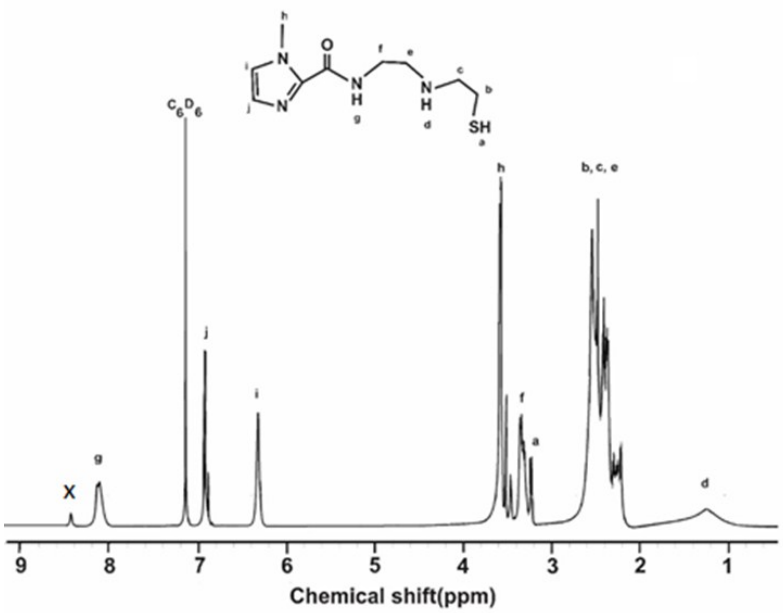

Figure S2. ^{1}H NMR of H_2L^3: (C_6D_6, 400 MHz) δ 1.35 (br, 1H), 2.3-2.7 (m, 6H), 3.2-3.5 (m, 3H), 3.68 (s, 3H), 6.32 (d, 1H), 6.92 (d, 1H), 8.08 (s, 1H). The small peak labeled x results from tautomerization of the amido proton (g). Addition of D_2O results in the loss of this peak.

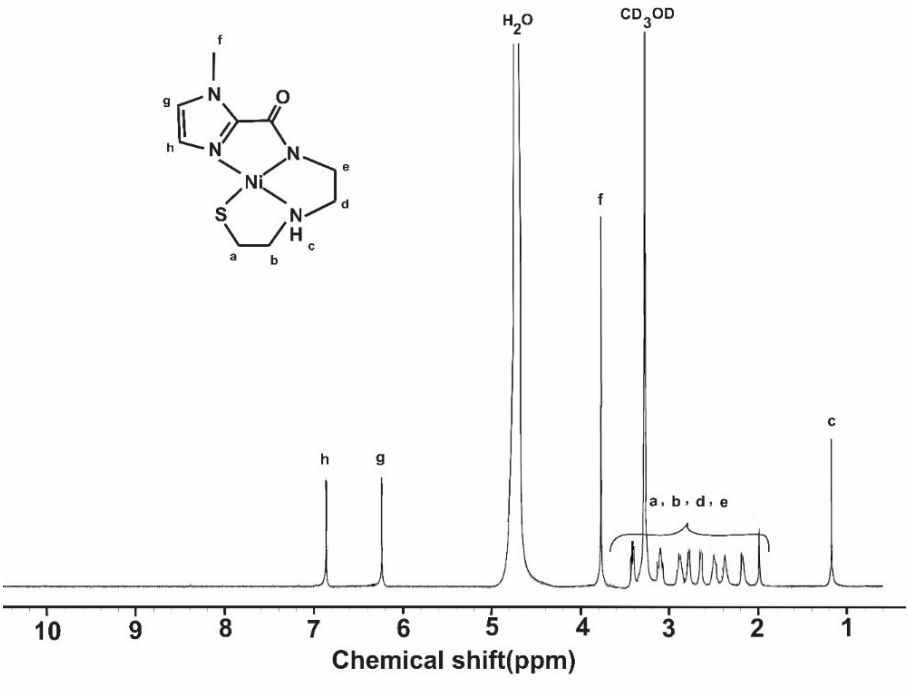

Figure S3. ^{1}H NMR of NiL^3 (**2**): (CD_3OD, 400 MHz) δ 1.18 (s, 1H), 2.16-3.45 (m, 8H), 3.78 (s, 3H), 6.29 (d, 1H), 6.92 (d, 1H).

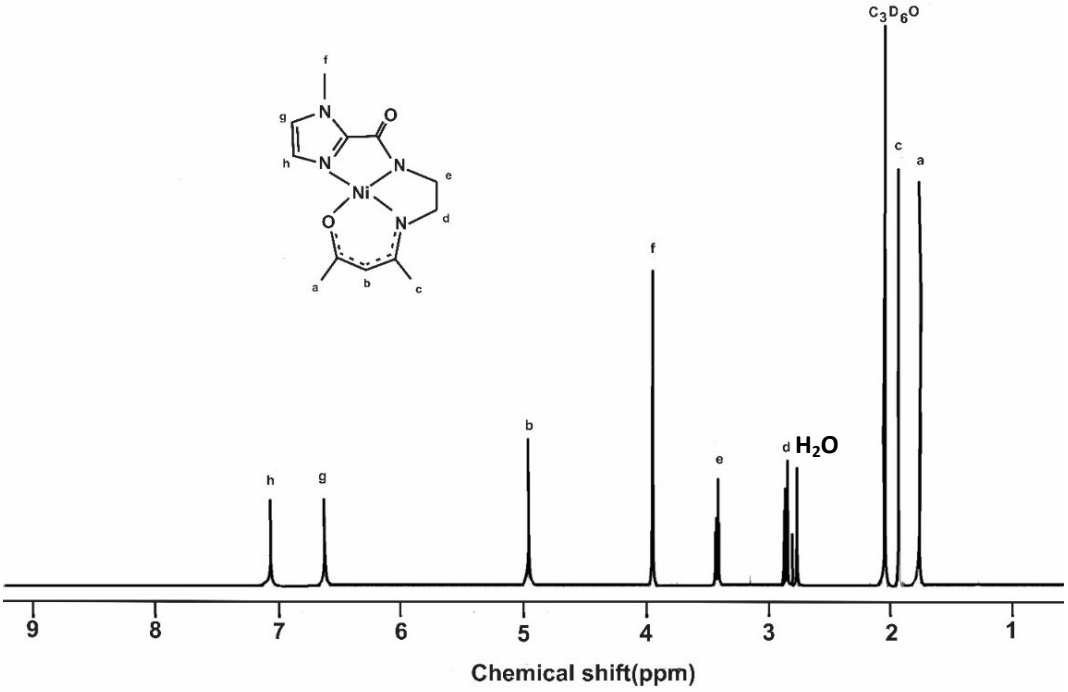

Figure S4. ^{1}H NMR of NiL^4 (**4**): (C_3D_6O, 400 MHz) δ 1.77 (s, 3H), 1.90 (s, 3H), 2.84 (t, 2H), 3.41 (t, 2H), 3.92 (s, 3H), 4.98 (s, 1H), 6.61 (d, 1H), 7.05 (d, 1H).

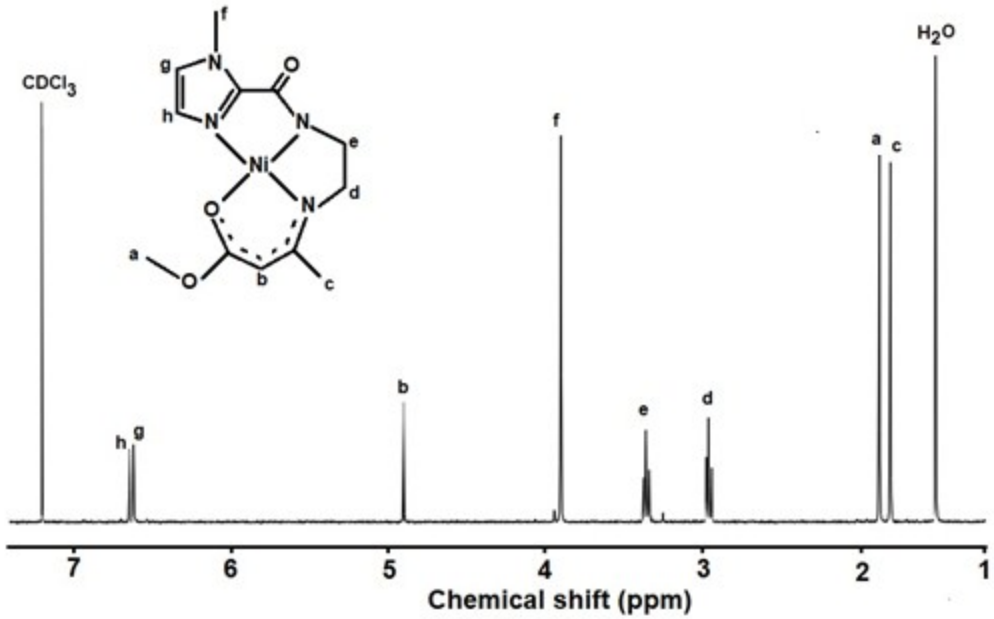

Figure S5. ^{1}H NMR of NiL^5 (**5**): ($CDCl_3$, 400 MHz) δ 1.78 (s, 3H), 1.82 (s, 3H), 2.92 (t, 2H), 3.45 (t, 3H), 3.88 (s, 3H), 4.86 (s, 1H), 6.62 (d, 1H), 6.64 (d, 1H).

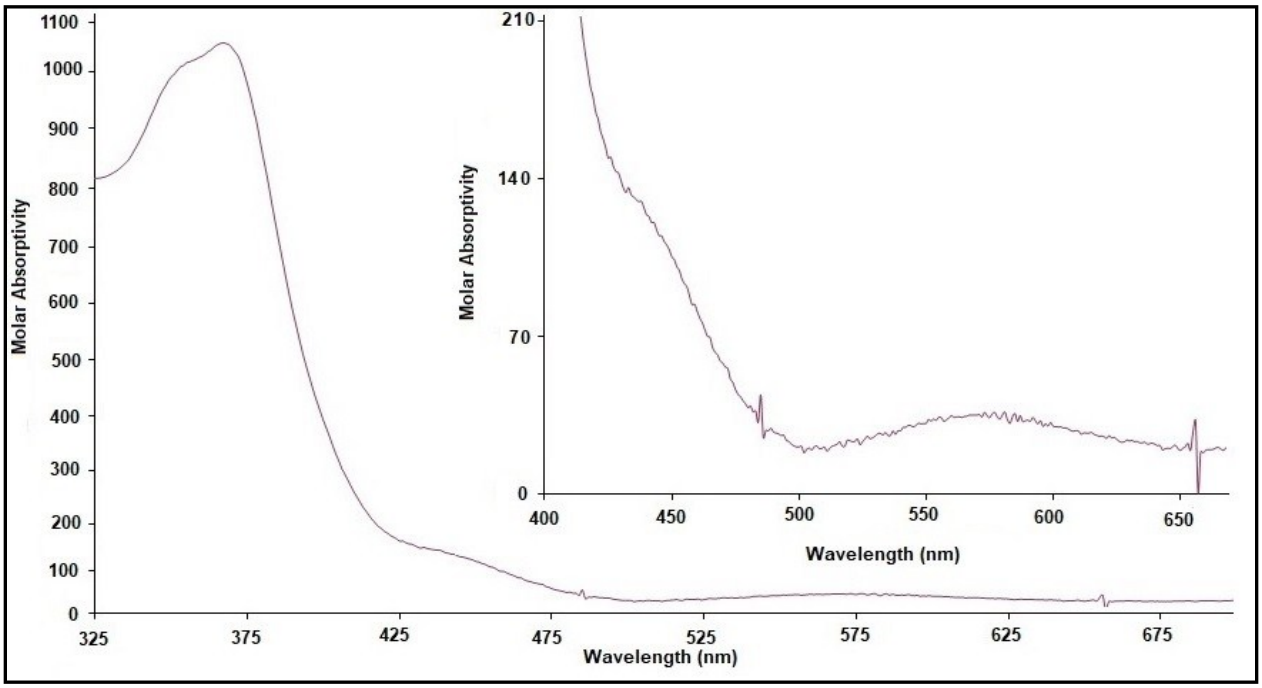

Figure S6. UV-Vis spectrum of NiL^3 (**2**) in CH_3CN.

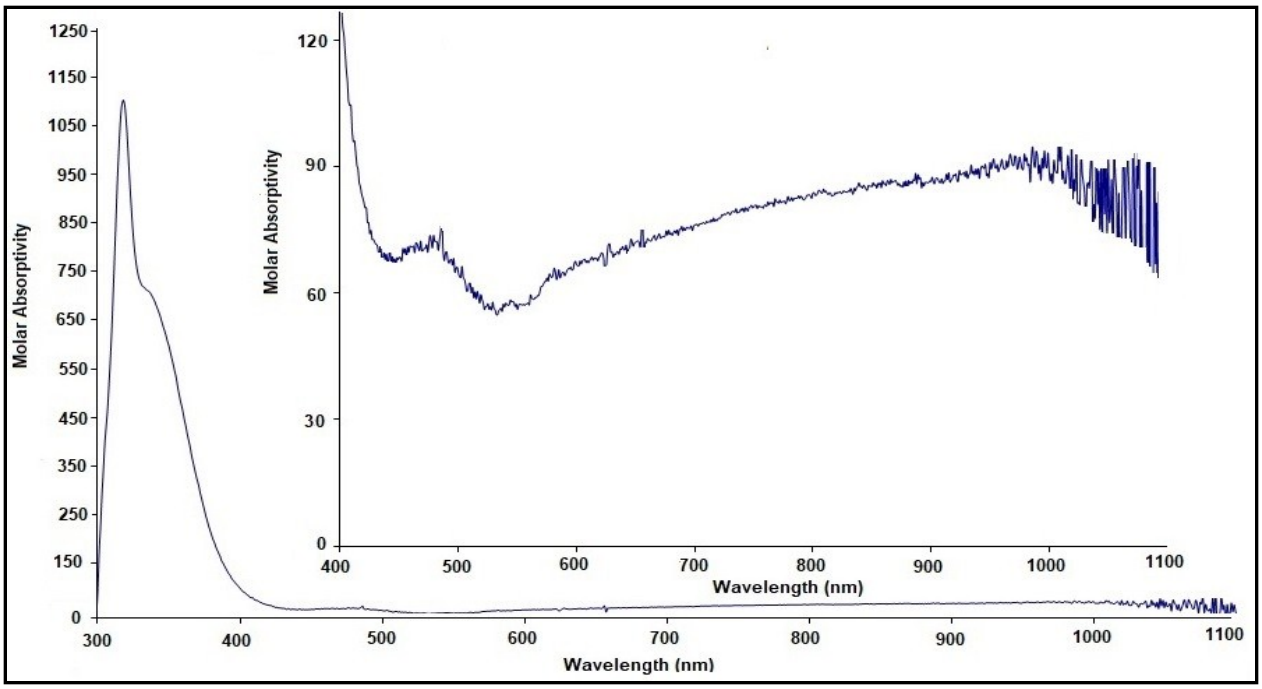

Figure S7. UV-Vis spectrum of $Ni(L^1)_2$ (**3**) in CH_2Cl_2.

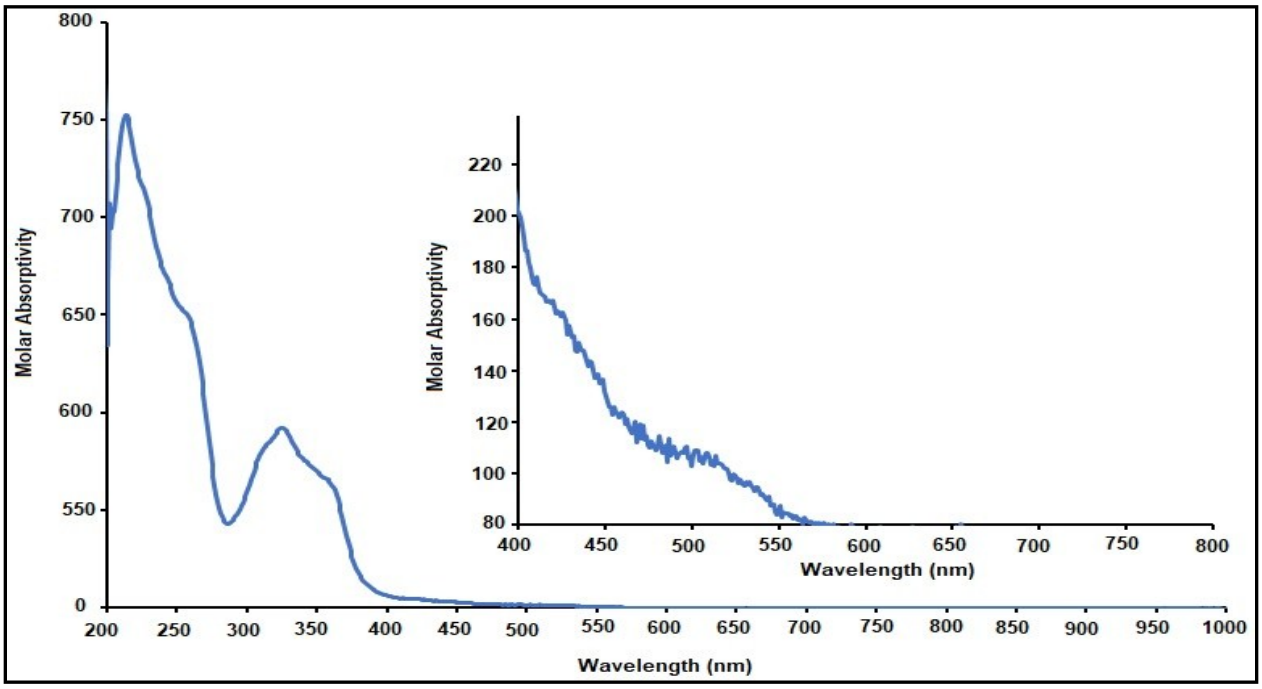

Figure S8. UV-Vis spectrum of NiL^4 (**4**) in CH_3CN.

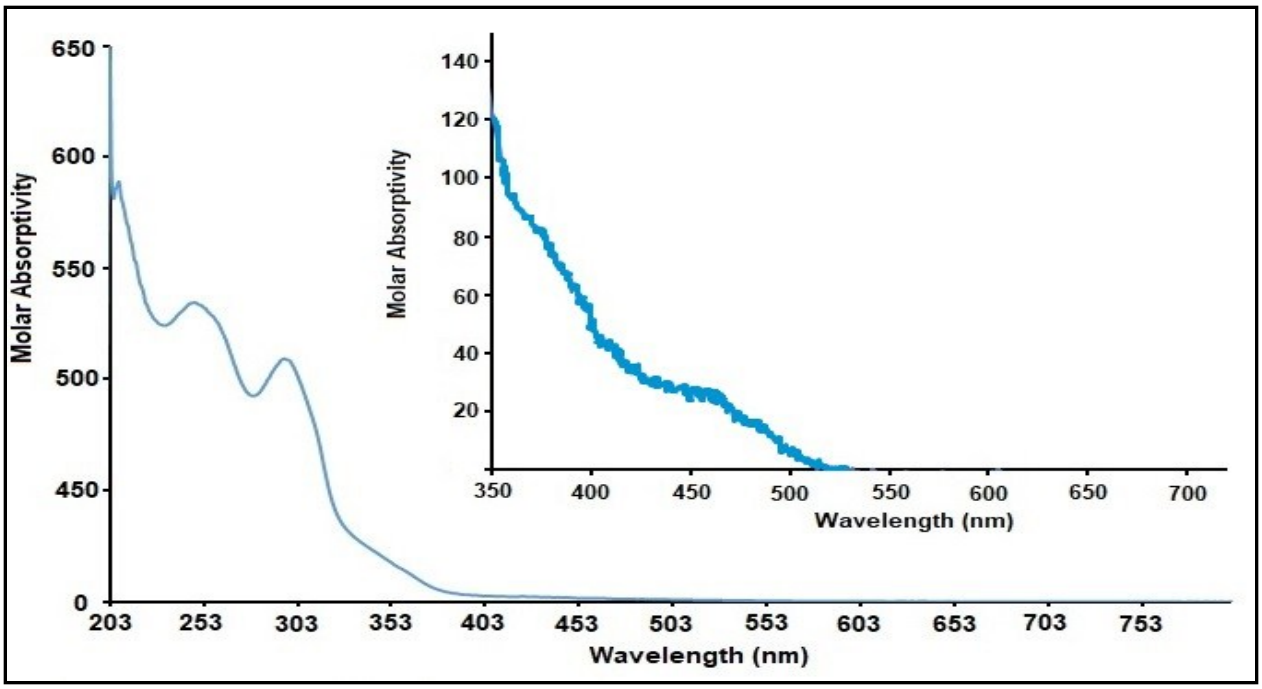

Figure S9. UV-Vis spectrum of NiL^5 (**5**) in CH_3CN.

Table S1. Selected stretches (cm^{-1}) in FT-IR spectra of HL^1 and **1-5**

Moiety	**HL^1**	**1**	**2**	**3**	**4**	**5**
C = O	1670	1660	1660	1590	1610	1590
C — N	1544	1540	1540	1510	1510	1510

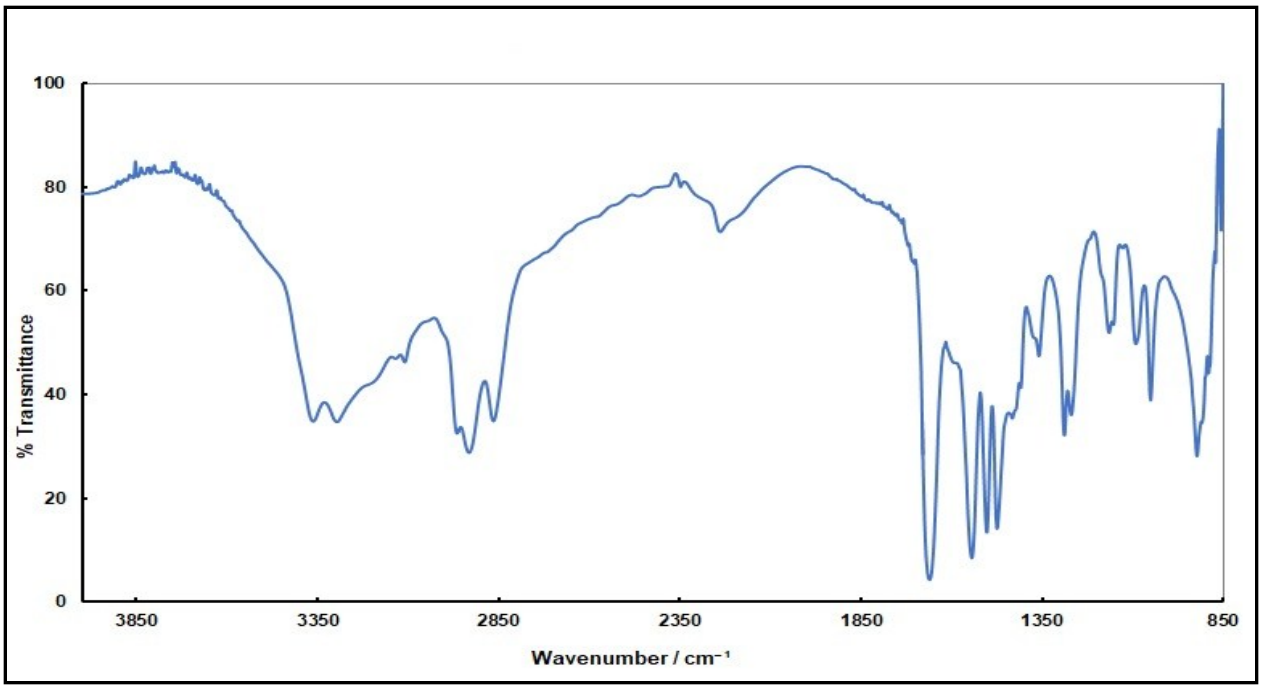

Figure S10. FT-IR spectrum of HL[1].

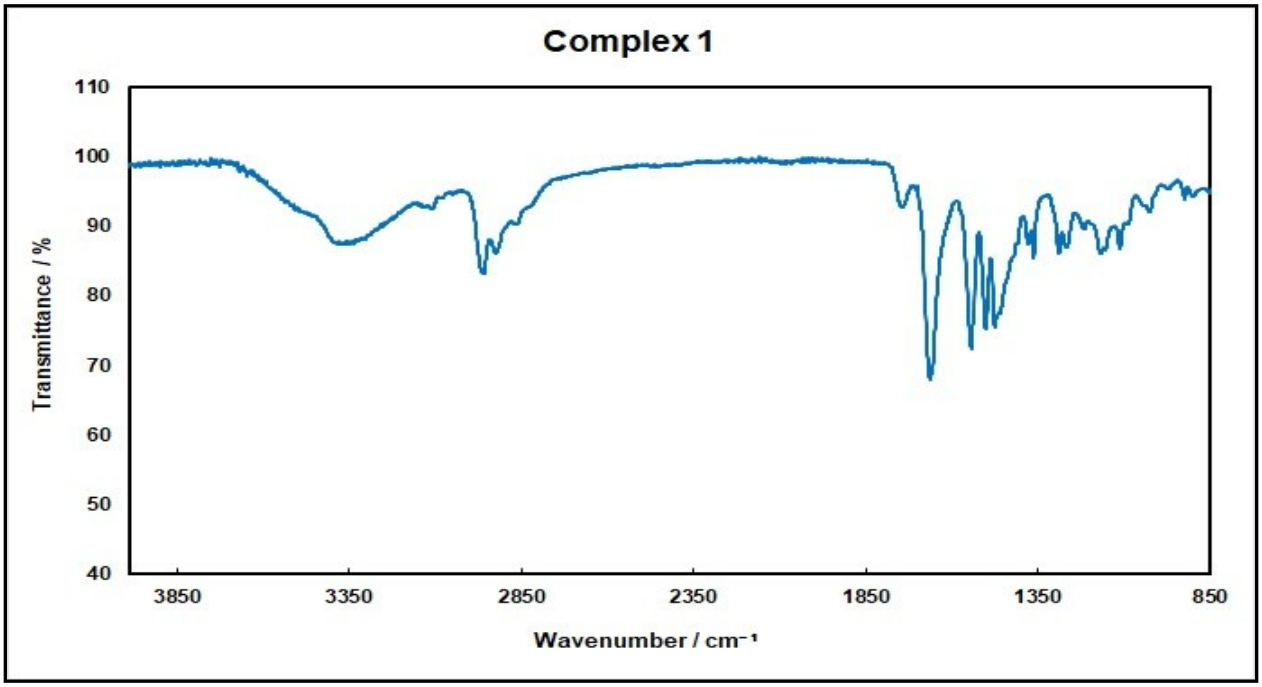

Figure S11. FT-IR spectrum of NiL[2] (**1**).

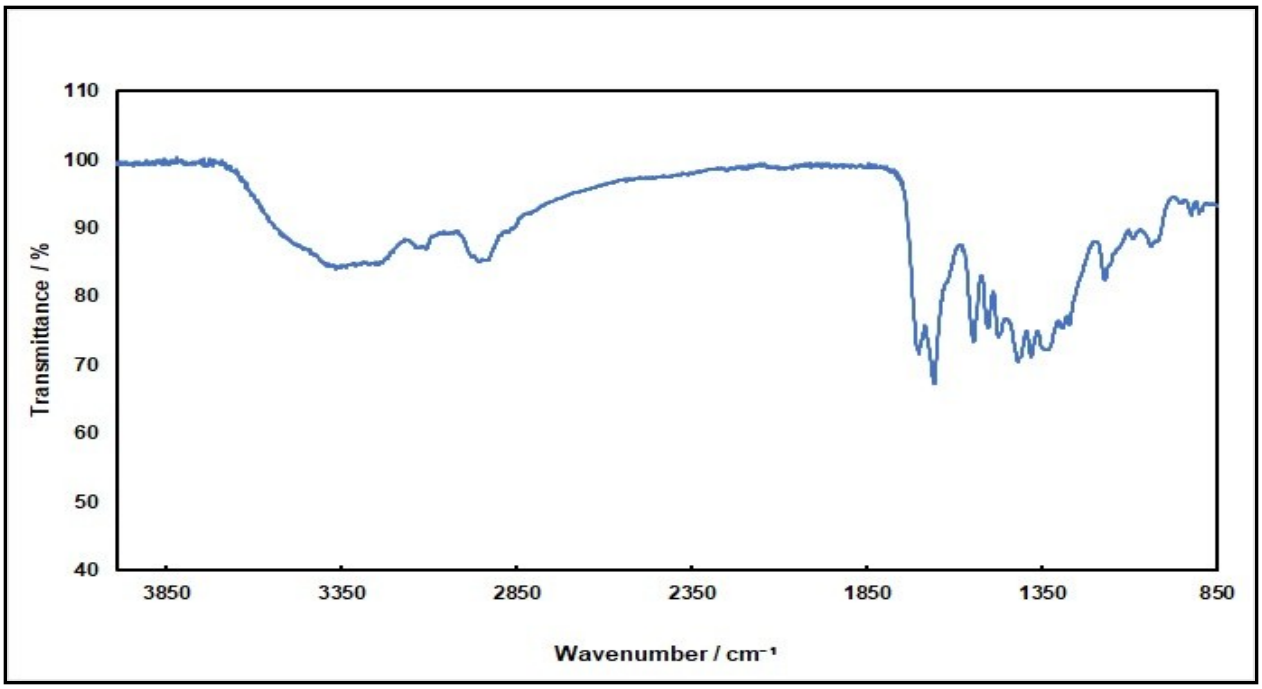

Figure S12. FT-IR spectrum of NiL^3 (**2**).

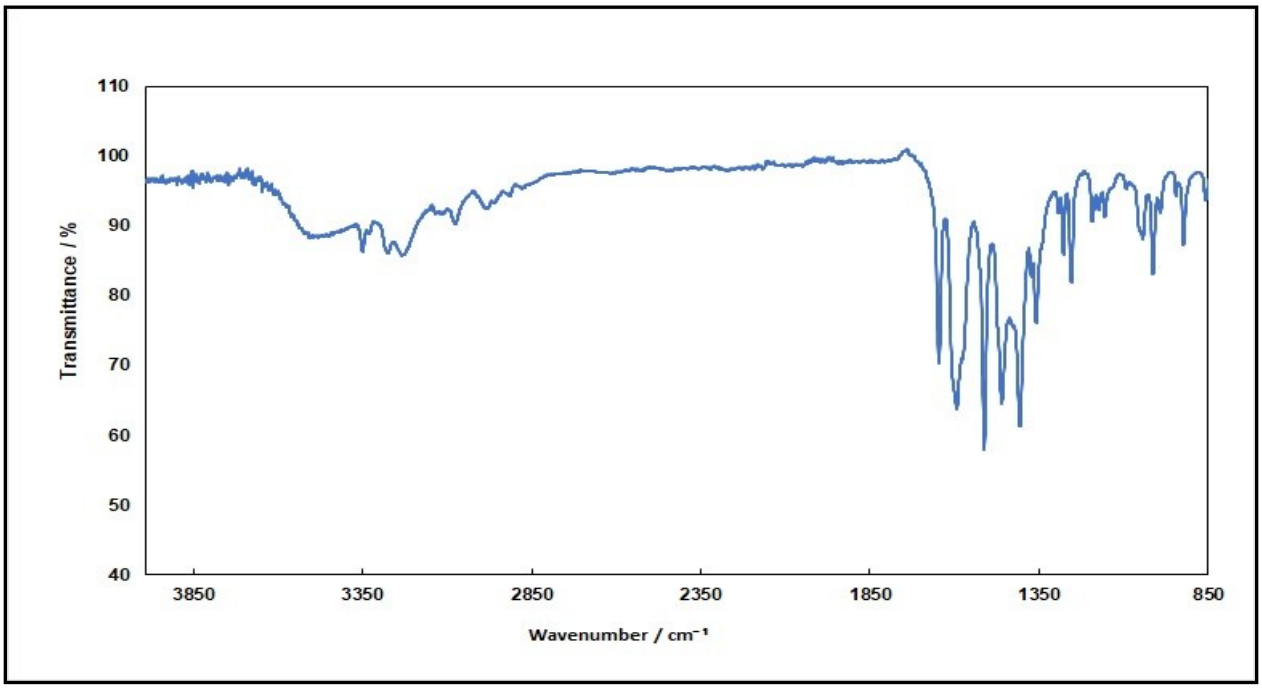

Figure S13. FT-IR spectrum of $Ni(L^1)_2$ (**3**).

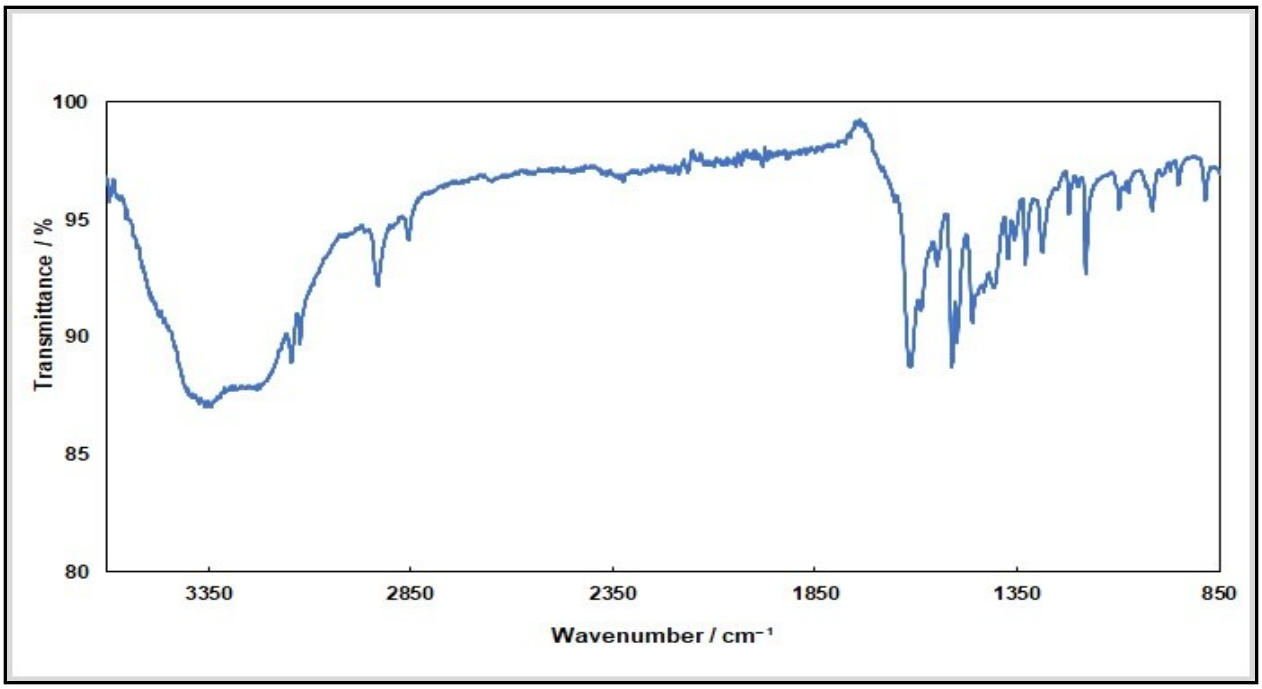

Figure S14. FT-IR spectrum of NiL^4 (**4**).

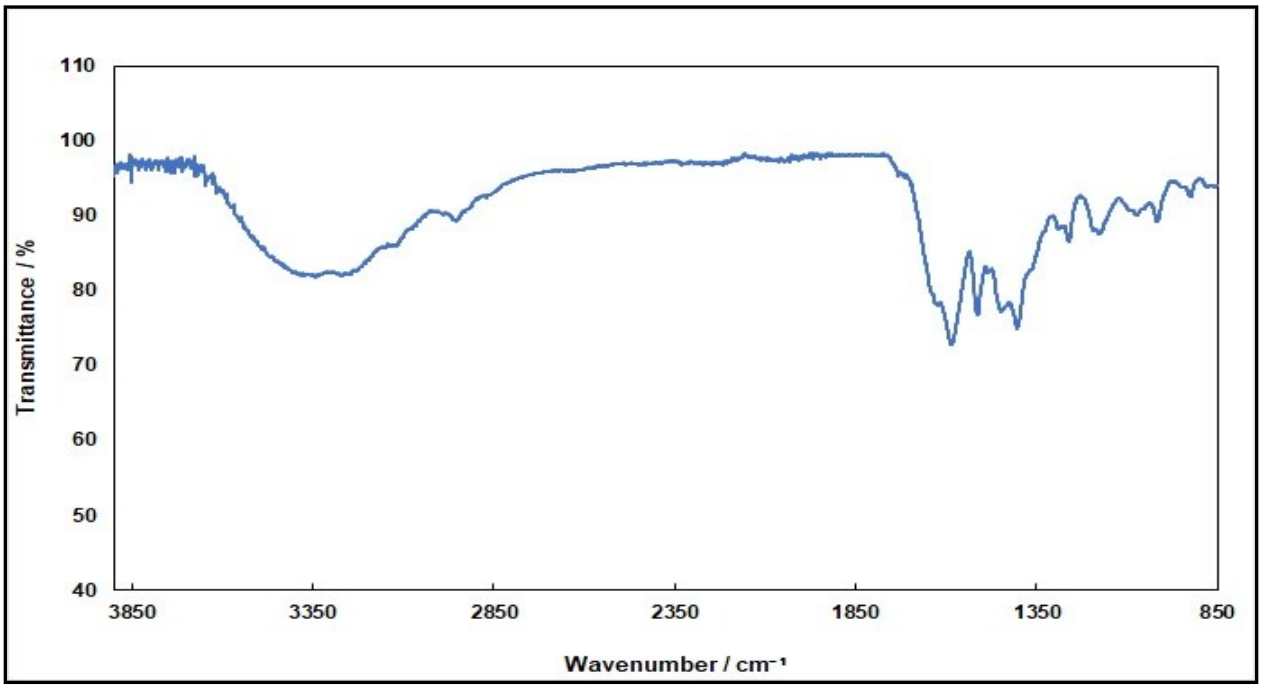

Figure S15. FT-IR spectrum of NiL^5 (**5**).

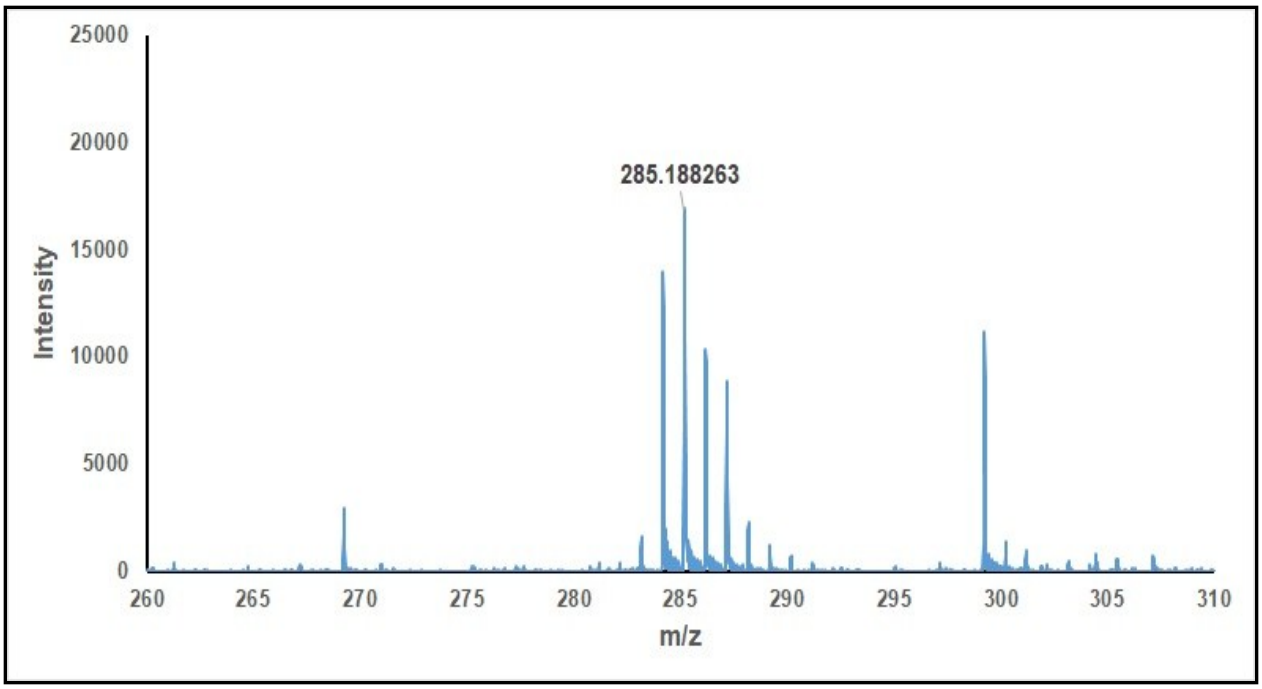

Figure S16. MALDI of NiL^3 (**2**).

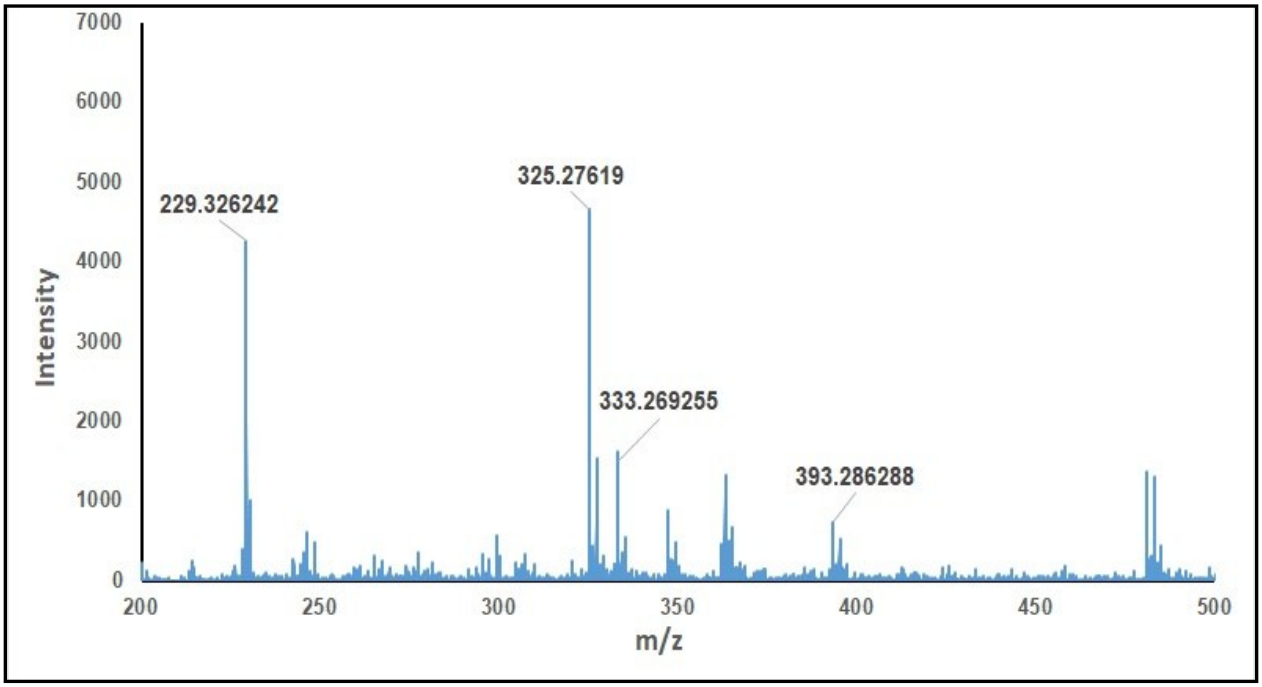

Figure S17. MALDI of $Ni(L^1)_2$ (**3**).

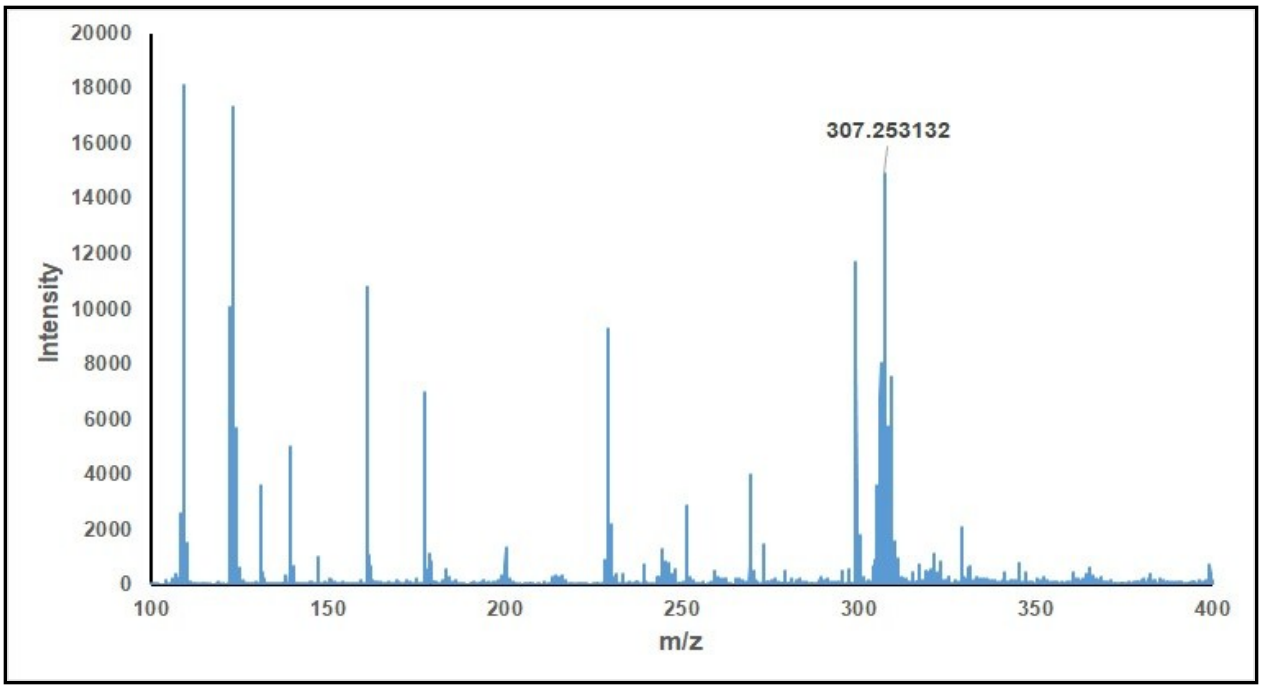

Figure S18. MALDI of NiL^4 (**4**).

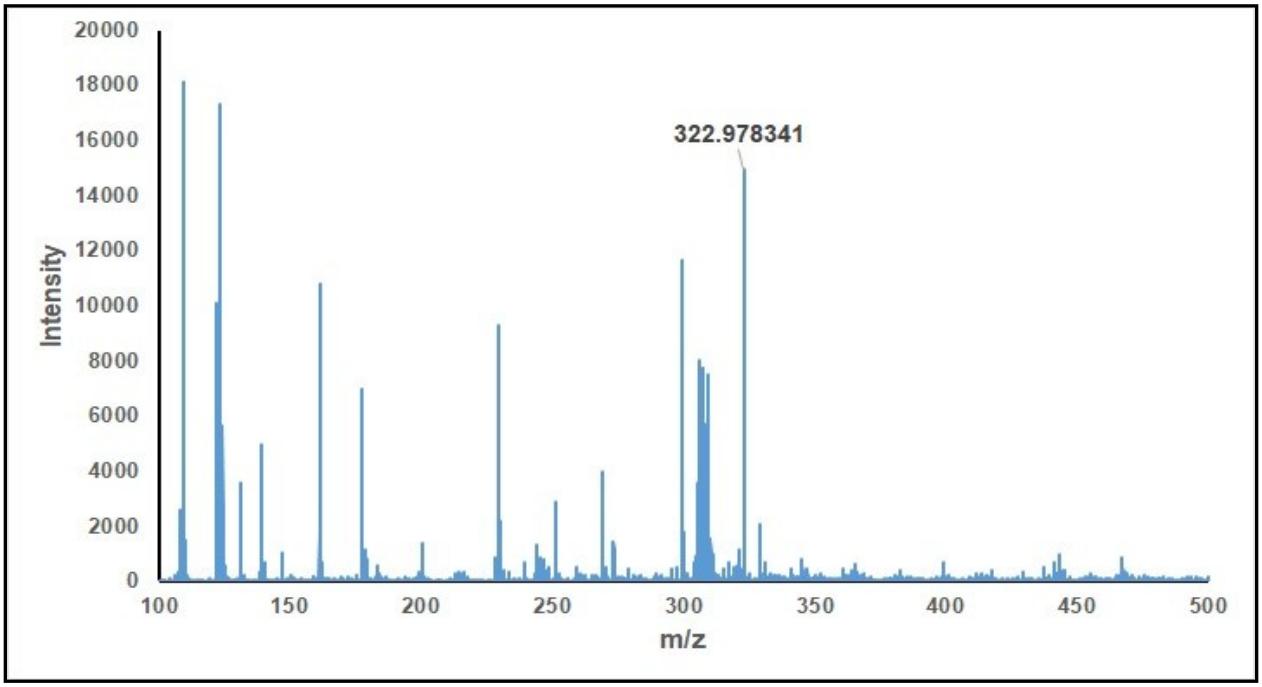

Figure S19. MALDI of NiL^5 (**5**).

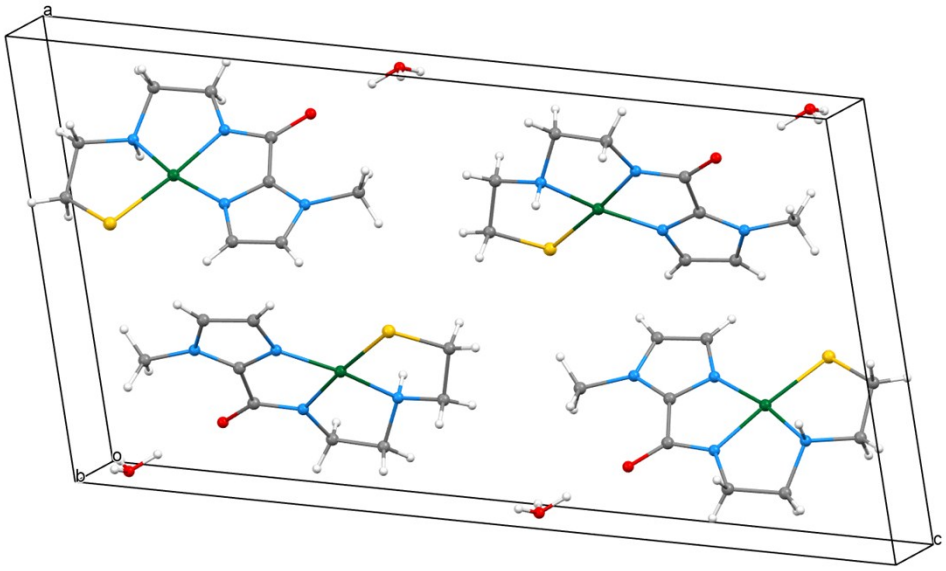

Figure S20. Unit cell diagram of NiL^3 (**2**).

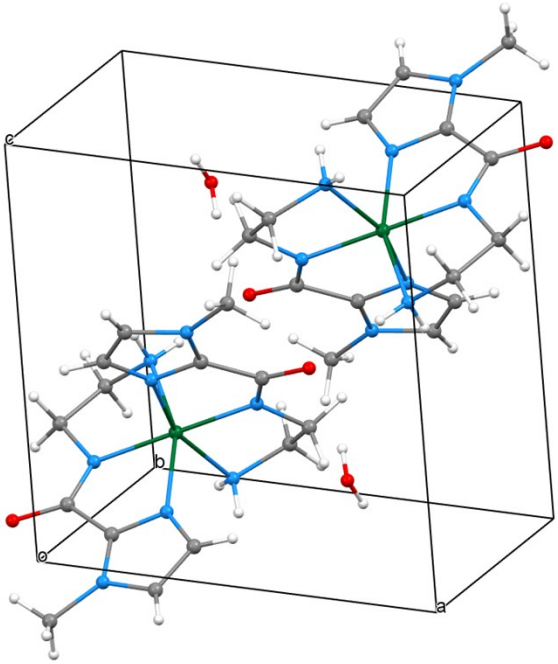

Figure S21. Unit cell diagram of $Ni(L^1)_2$ (**3**).

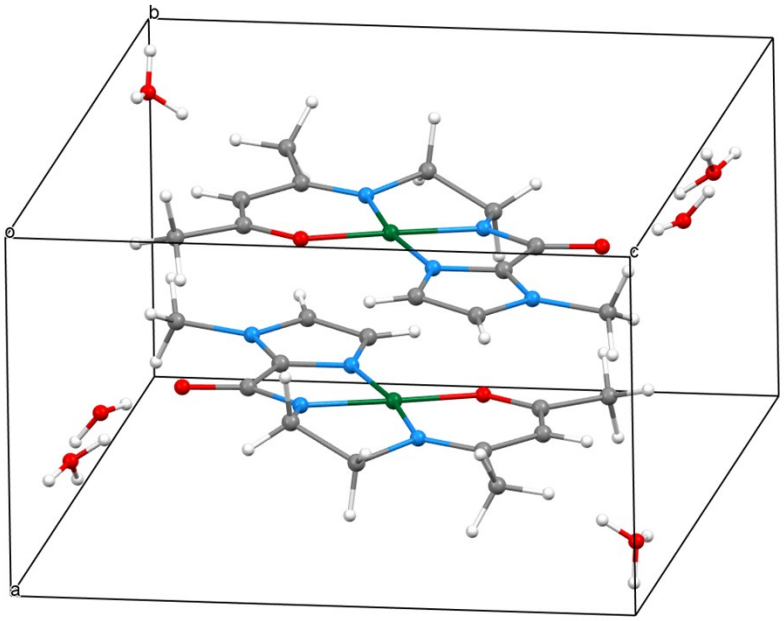

Figure S22. Unit cell diagram of NiL^4 (**4**).

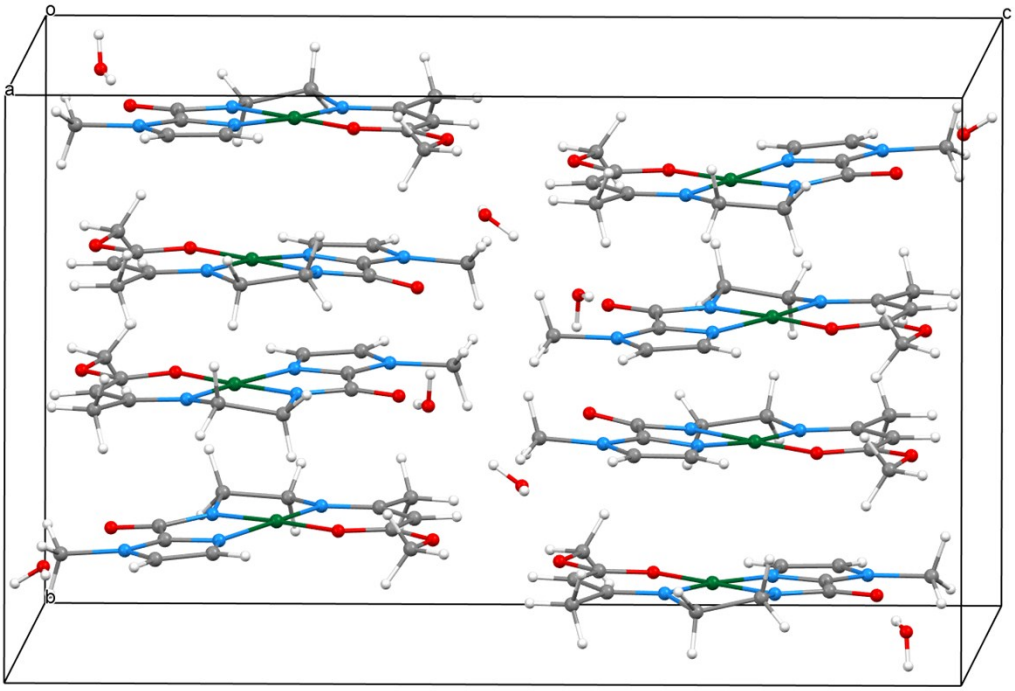

Figure S23. Unit cell diagram of NiL^5 (**5**).

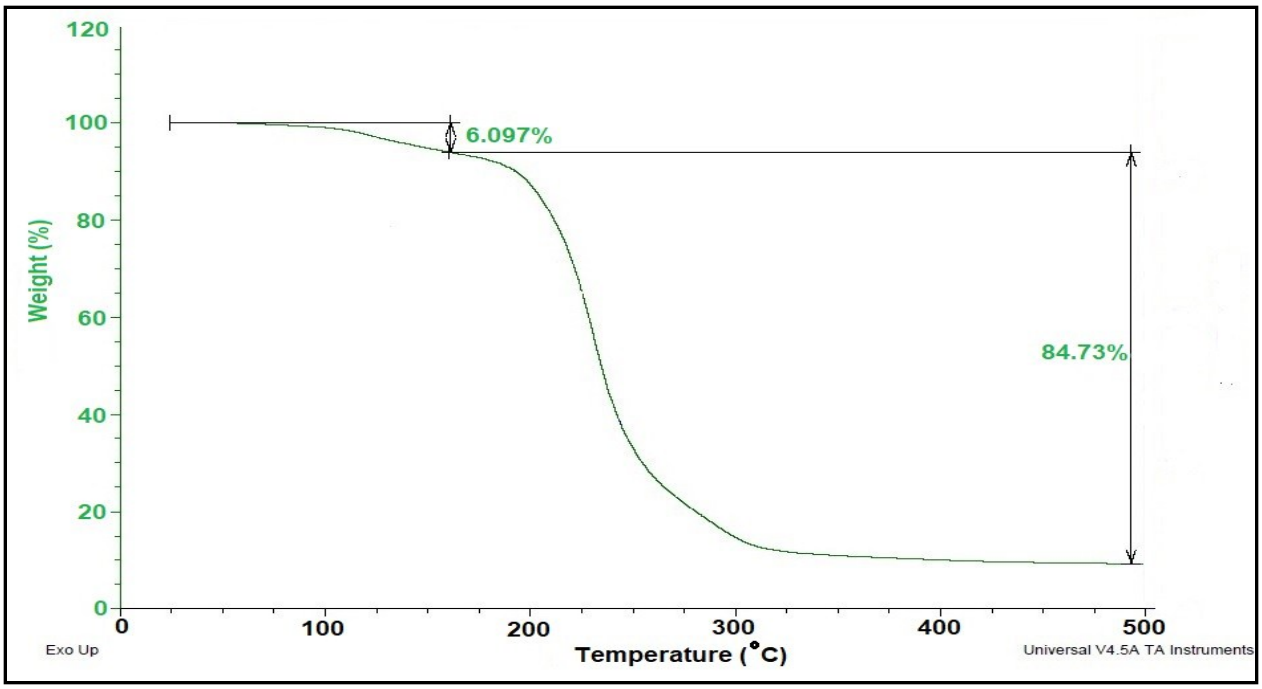

Figure S24. TGA of NiL^2 (**1**).

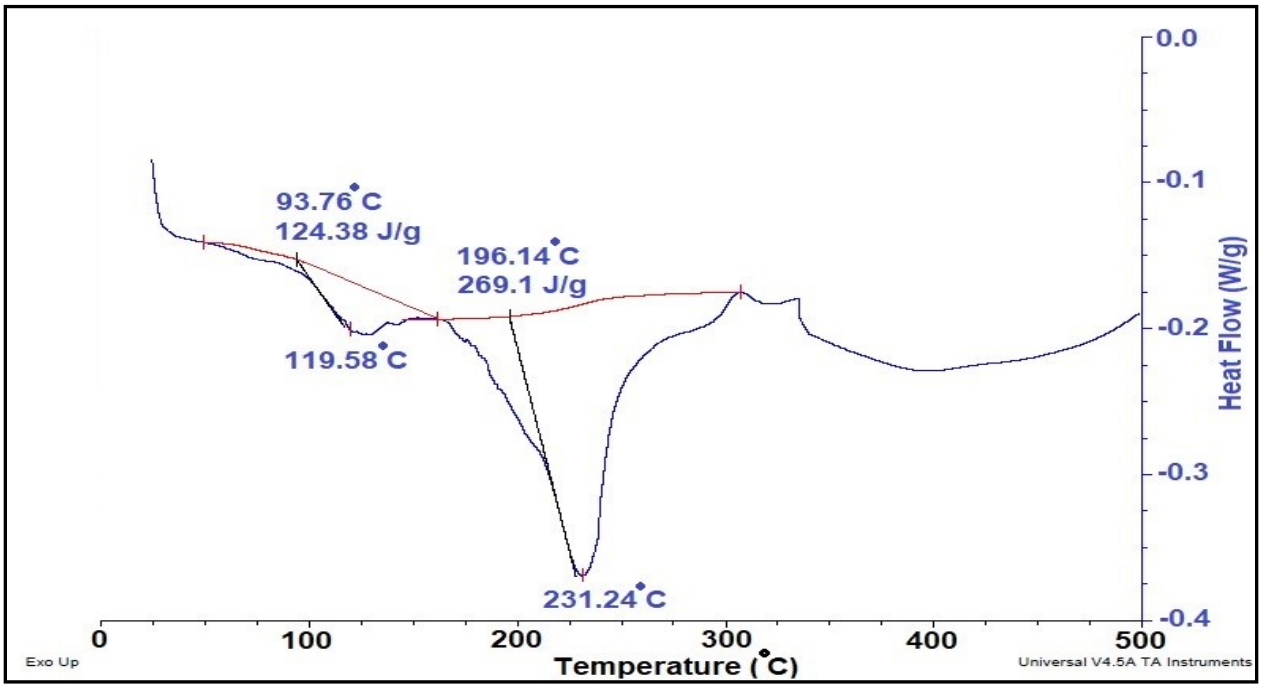

Figure S25. DSC of NiL^2 (**1**).

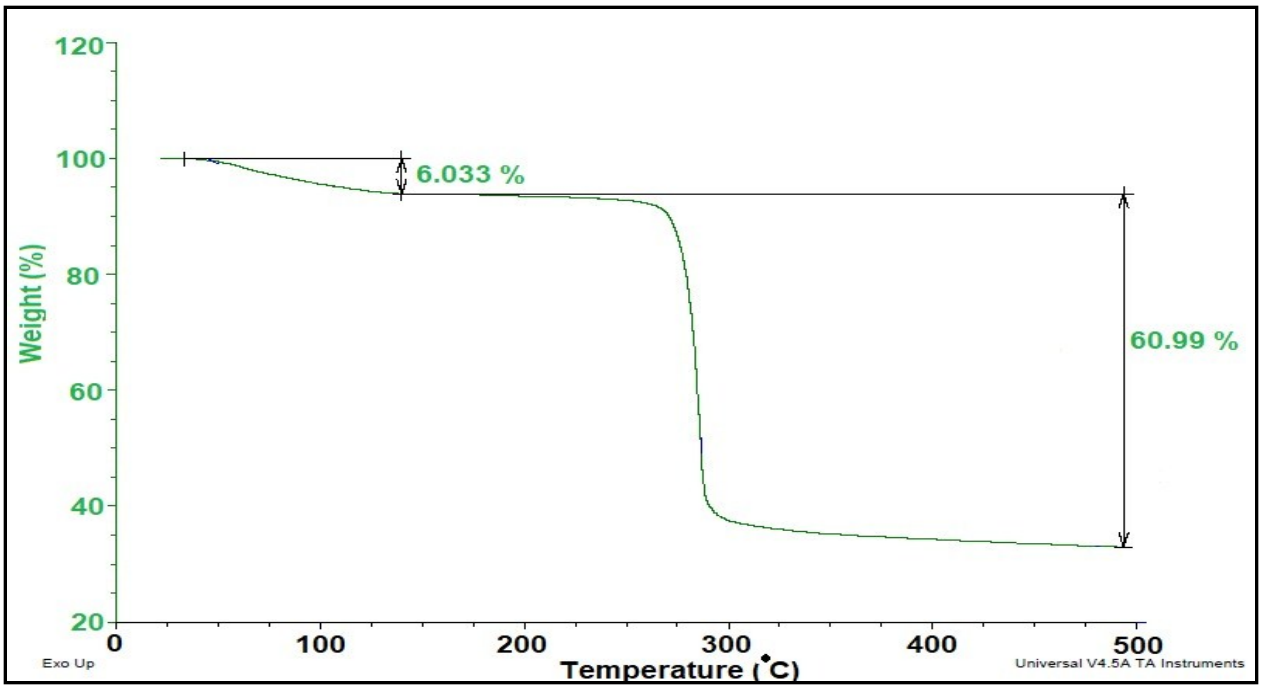

Figure S26. TGA of NiL^3 (**2**).

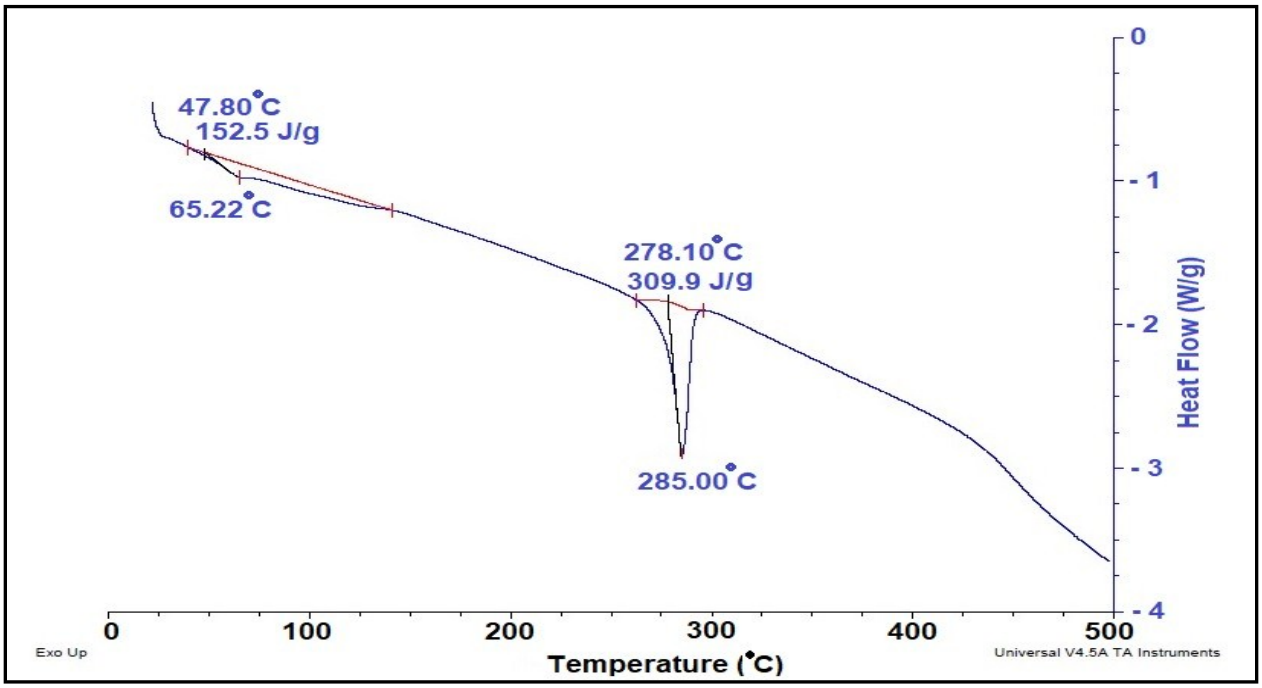

Figure S27. DSC of NiL^3 (**2**).

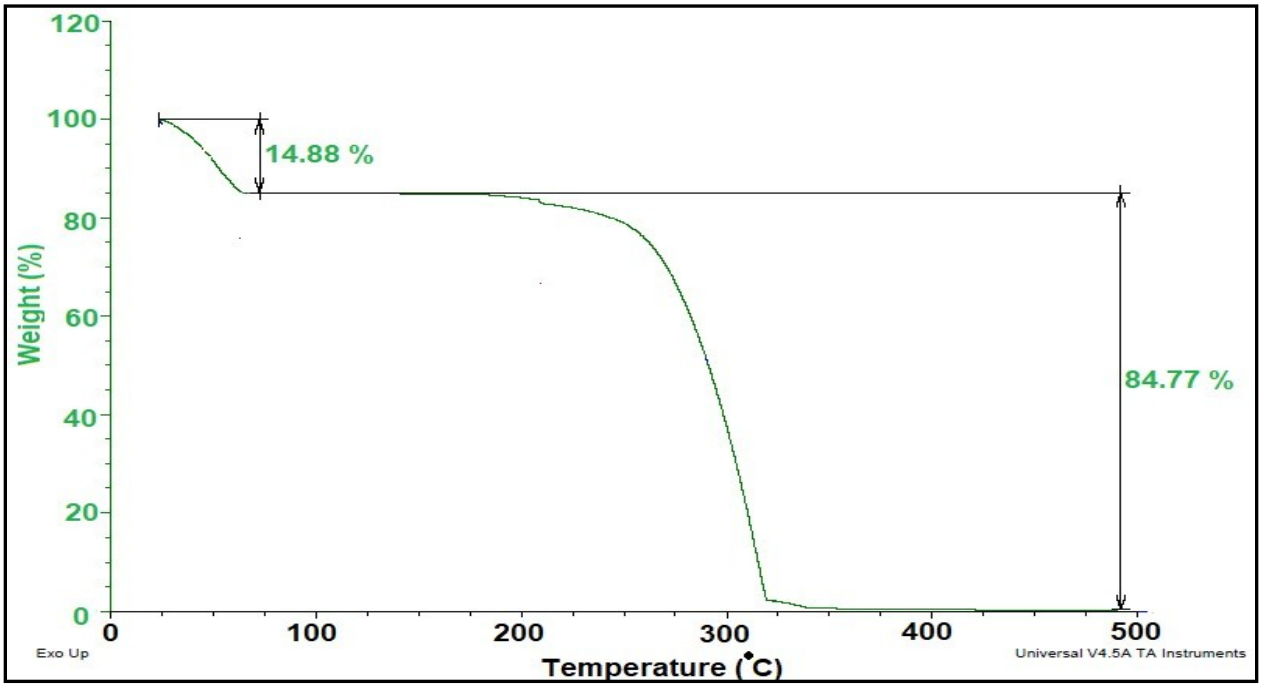

Figure S28. TGA of NiL^4 (**4**).

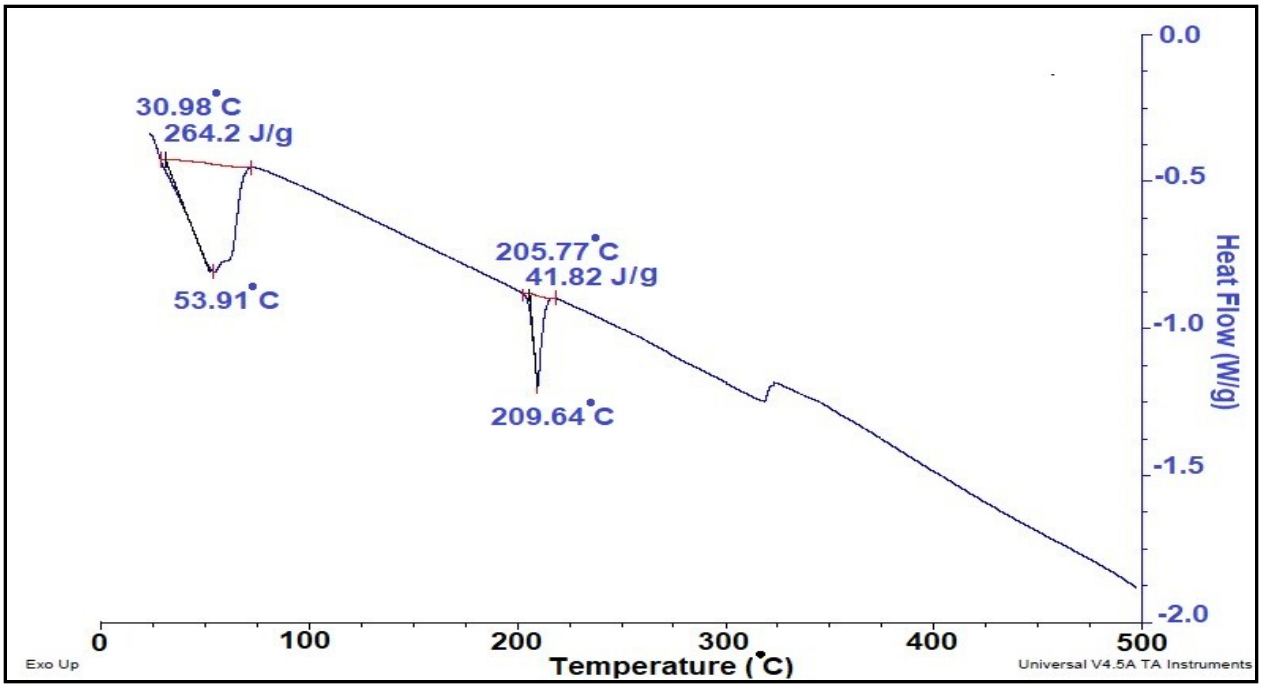

Figure S29. DSC of NiL^4 (**4**).

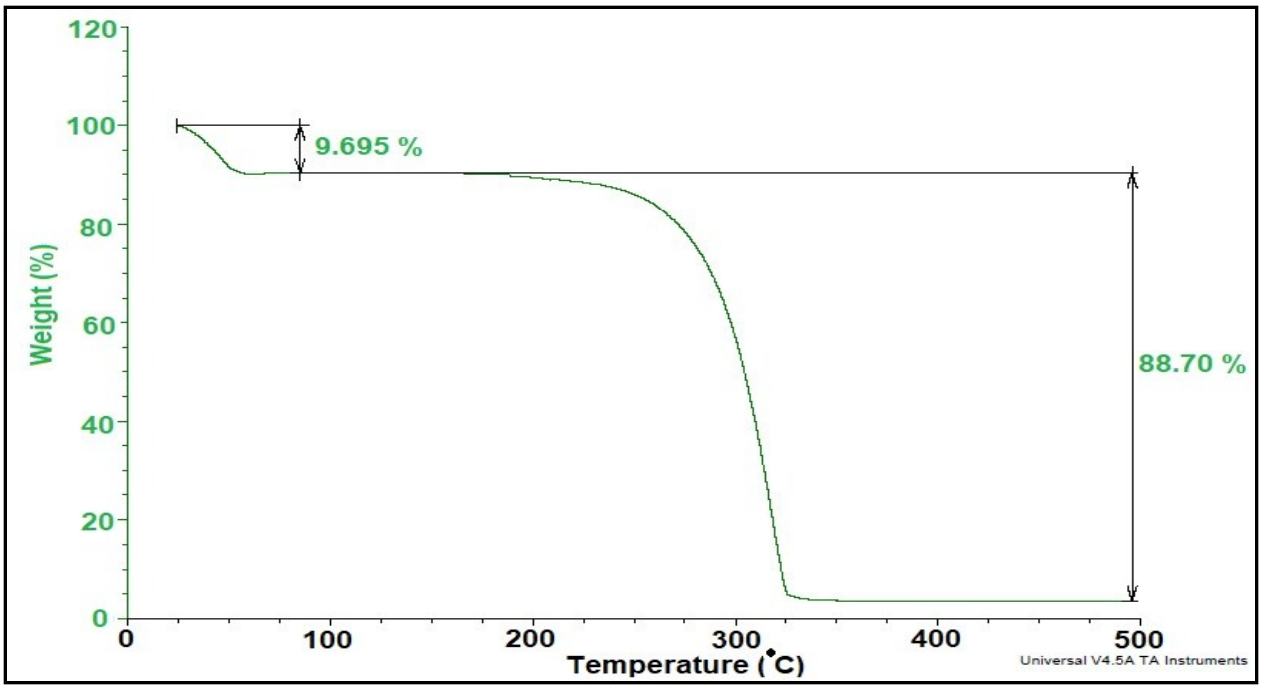

Figure S30. TGA of NiL[5] (**5**).

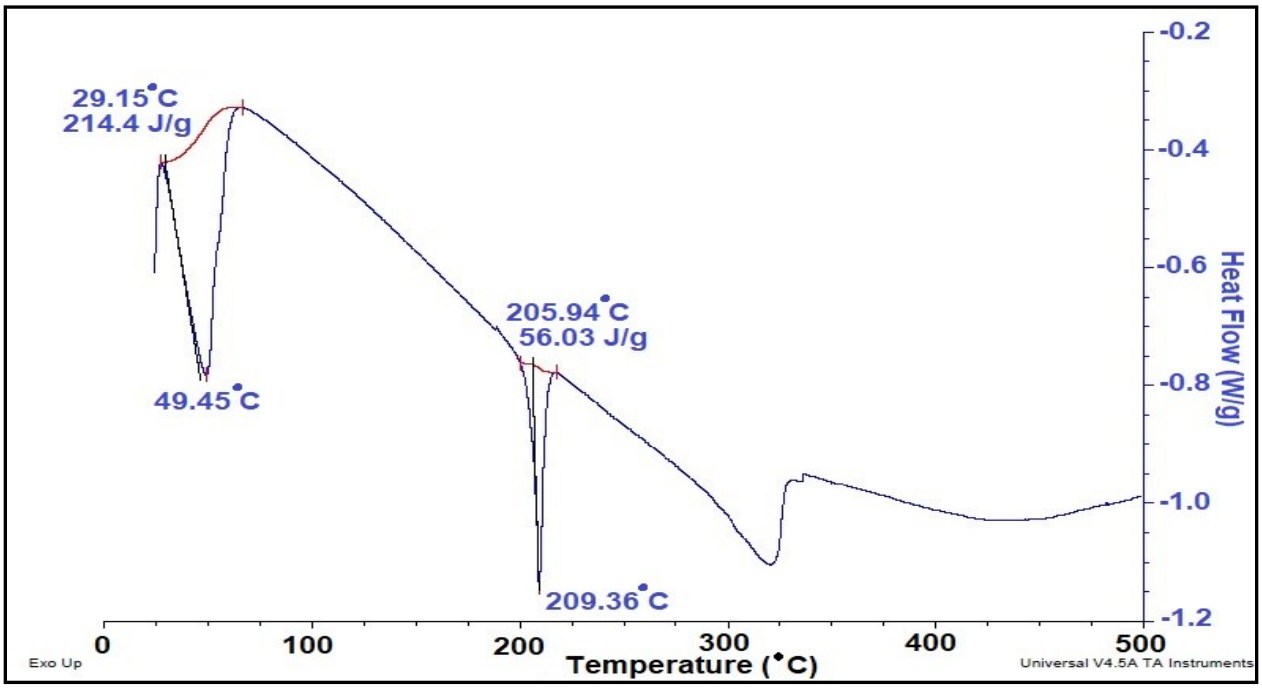

Figure S31. DSC of NiL[5] (**5**).

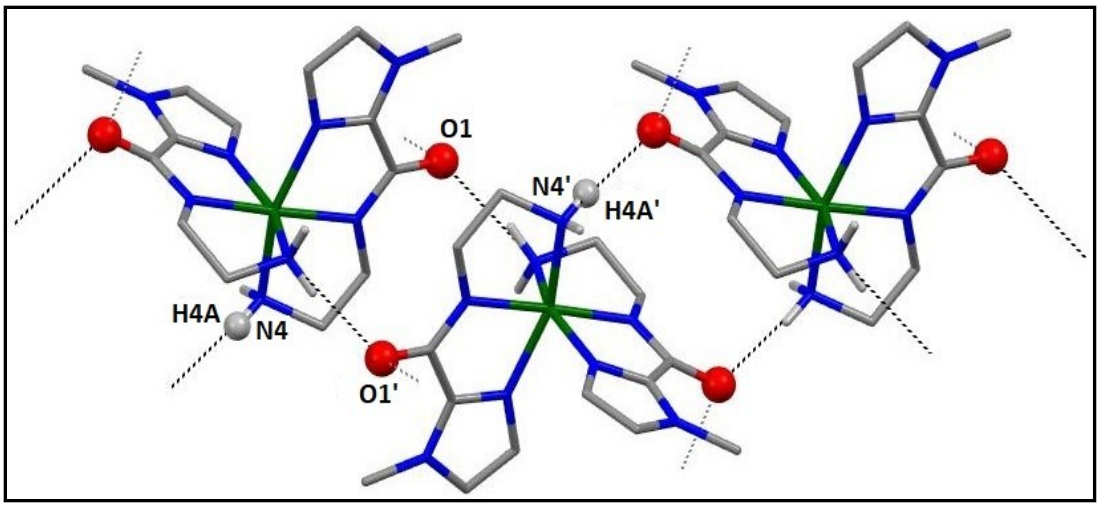

Figure S32. $C^2_2(12)$ HB motif in $Ni(L^1)_2$ (**3**).

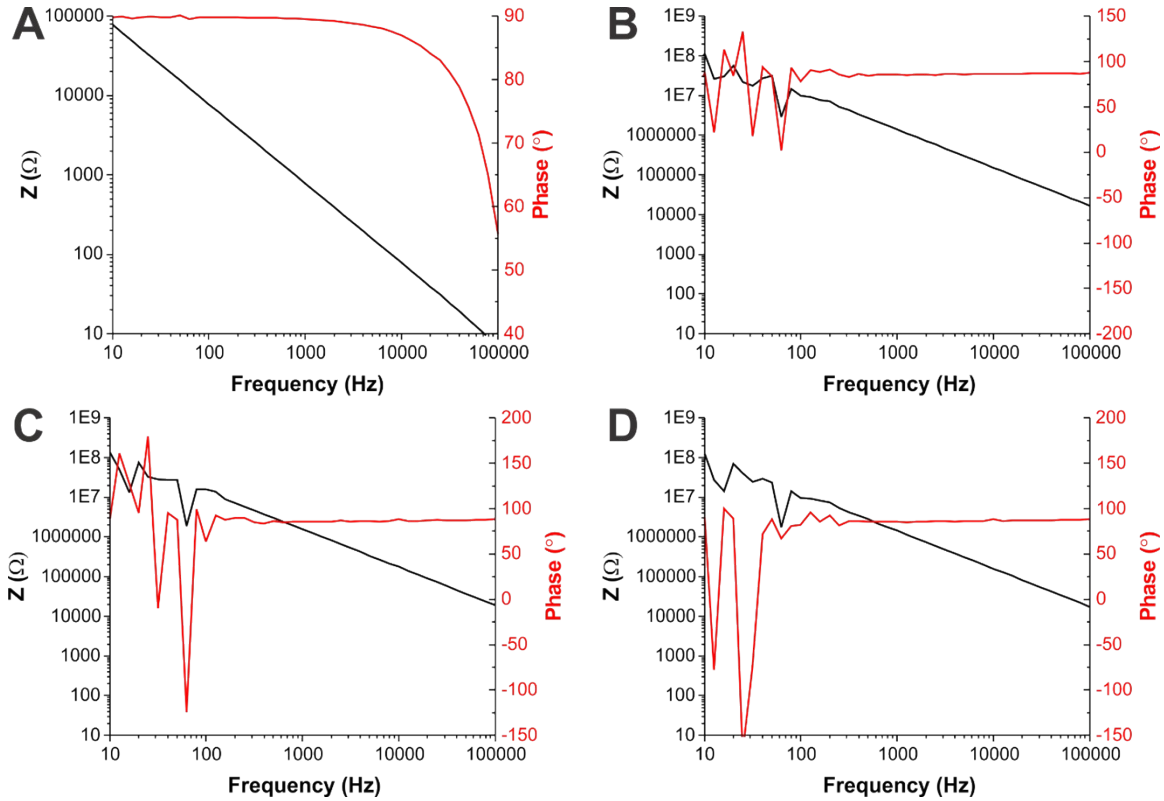

Figure S33. Bode representations of EIS data for 22 µF capacitor control (A), complexes **1** (B), **4** (C), and **5** (D). Shows the phase angle and impedance behavior as a function of frequency. The inverse relation between Z and frequency and constant ~90 ° phase angles in all four plots are characteristics of capacitors..

Table S2. Capacitances (with associated chi-squared values) and Z' at 100 kHz (indicative of equivalent series resistance) for the capacitor control and complexes **1**, **4**, and **5** at various applied DC biases. Also depicted is the equivalent circuit model used to fit EIS data and determine capacitance.

Sample	DC Bias (V)	Circuit	Chi-Squared	Capacitance (F)	Z' @ 100 kHz (Ω)
Capacitor	-0.1	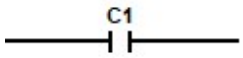	1E-20	2.08E-07	3.84
	0		1E-20	2.08E-07	3.82
	0.1		1E-20	2.07E-07	6.63
Complex 1	-0.1		1E-20	1.31E-10	1346.88
	0		1E-20	1.25E-10	729.26
	0.1		1E-20	1.30E-10	984.91
Complex 4	-0.1		1E-20	1.07E-10	659.57
	0		1E-20	1.12E-10	650.04
	0.1		1E-20	1.07E-10	637.31
Complex 5	-0.1		1E-20	1.23E-10	512.69
	0		1E-20	1.27E-10	577.06
	0.1		1E-20	1.33E-10	529.32

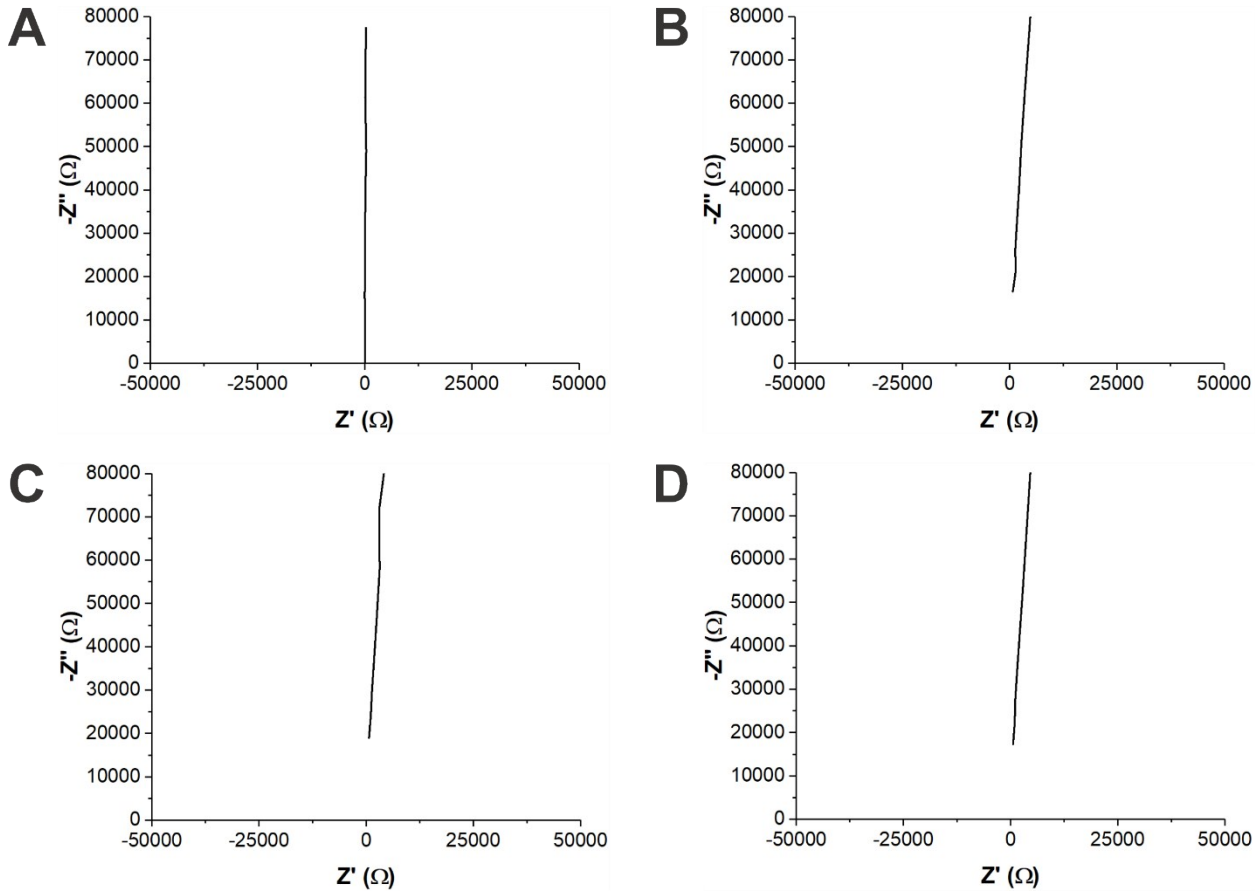

Figure S34. Nyquist representations of EIS data for 22 μF capacitor control (A), complexes **1** (B), **4** (C), and **5** (D). Data in B, C, and D were truncated at -Z'' = 80,000 Ω to illustrate similarities with (A) and omit the diffusion-related noise observed at low frequencies.